# 3D-printed SAPO-34 monoliths for gas separation

Couck, Sarah; Cousin-Saint-Remi, Julien; Van der Perre, Stijn; Baron, Gino V.; Minas, Clara; Ruch, Patrick; Denayer, Joeri F.M.

*Published in:*
Microporous and Mesoporous Materials

*DOI:*
10.1016/j.micromeso.2017.07.014

*Publication date:*
2018

Microporous and Mesoporous Materials 255 (2018) 185–191

Contents lists available at ScienceDirect

Microporous and Mesoporous Materials

journal homepage: www.elsevier.com/locate/micromeso

# 3D-printed SAPO-34 monoliths for gas separation

Sarah Couck [a], Julien Cousin-Saint-Remi [a], Stijn Van der Perre [a], Gino V. Baron [a], Clara Minas [b], Patrick Ruch [c], Joeri F.M. Denayer [a, *]

[a] Chemical Engineering Department, Vrije Universiteit Brussel, Pleinlaan 2, 1050 Brussel, Belgium
[b] Complex Materials, Department of Materials, ETH Zürich, Vladimir-Prelog-Weg 5, 8093 Zürich, Switzerland
[c] IBM Research – Zurich, Säumerstrasse 4, 8803 Rüschlikon, Switzerland

ARTICLE INFO

*Article history:*
Received 31 March 2017
Received in revised form
5 July 2017
Accepted 7 July 2017
Available online 8 July 2017

*Keywords:*
SAPO-34
Monolith
3D printing
Adsorption
Gas separation
$CO_2$ capture

ABSTRACT

A 3D printing method (the Direct Ink writing, DIW, method) is applied to produce SAPO-34 zeolite based structured adsorbents with the shape of a honeycomb-like monolith. The use of the 3D printing technique gives this structure a well-defined and easily adaptable geometry. As binder material, methyl cellulose was used. The SAPO-34 monolith was characterized by SEM as well as Ar and Hg porosimetry. The $CO_2$ adsorption affinity, capacity and heat of adsorption were determined by recording high pressure adsorption isotherms at different temperatures, using the gravimetric technique. The separation potential was investigated by means of breakthrough experiments with mixtures of $CO_2$ and $N_2$. The experimental selectivity of $CO_2/N_2$ separation was compared to the selectivity as predicted by the Ideal Adsorbed Solution Theory. A drop in capacity was noticed during the experiments and $N_2$ capacities were close to zero or slightly negative due to the very low adsorption, meaning absolute selectivity values could not be determined. However, due to the low $N_2$ capacity, experimental selectivity is estimated to be excellent as was predicted with IAST. While the 3D printing is found to be a practical, fast and flexible route to generate monolithic adsorbent structures, improvements in formulation are required in terms of sample robustness for handling purposes and heat transfer characteristics of the obtained monoliths during gas separation.



## 1. Introduction

In the past decade, it was demonstrated that structuring adsorbents into monolithic structures has some major advantages as compared to traditional shaped adsorbents like beads, granules or pellets. Monolithic structures lead to improvements in for example, pressure drop, mass transfer and/or heat transfer [1–6]. Such monolithic structures were mostly tested for $CO_2$ separation applications [7–13]. To prepare these monolithic structures, two main routes exist, e.g. direct extrusion of the adsorbent or attaching an adsorbent layer to a support monolith (for instance by means of wash-coating, dip-coating, or crystal growth). Apart from a limited flexibility, these methods of preparation do have some disadvantages. When using a support monolith with an adsorbent coating, a large part of the monolithic body does not contribute to the adsorption process and thus provides a poor volumetric yield of the adsorbent bed. Extruded monoliths on the other hand are prepared from the active material itself, but the shape of the resulting monolith is determined by the extrusion die, which has limited variability. Together with the high cost of the extrusion die, this restricts the possibilities to study the effect of structural properties (e.g. effect of wall thickness and channel width on mass and heat transfer) in a systematic way.

The emerging technique of 3D printing can offer a solution to the limitations of extrusion as it has a much higher level in freedom of operation. Therefore, it provides an excellent research tool, allowing to generate a wide variety in structures suitable for lab scale adsorption studies. 3D printing, also known as additive manufacturing, comprises several printing methods like fused deposition modelling (FDM), direct ink writing (DIW), stereolithography (SLA), selective laser sintering (SLS) and many more designations [14,15]. Although the first working 3D printer was already patented in 1984 (based on the SLA principle) [16], it is only recently that 3D printing has become a very popular commercial technique.

* Corresponding author.
*E-mail address:* joeri.denayer@vub.ac.be (J.F.M. Denayer).

http://dx.doi.org/10.1016/j.micromeso.2017.07.014
1387-1811/

Also in adsorption, catalysis or separation processes, this 3D printing technique is becoming a popular tool. In the field of heterogeneous catalysis, 3D printing has been applied to prepare a variety of structured catalysts as an alternative to honeycomb structures. Tubio et al. reported the 3D printing of a $Cu/Al_2O_3$ monolithic catalyst with excellent performance in the Ullmann reaction [17]. Michorczyk et al. described the generation of an Al based catalyst, by first printing the template very precisely with 3D printing, then filling the template with the catalyst and as a last step burning away the template, leaving a well-defined catalytic reactor [18]. Azuaje et al. reported the direct printing of an Al catalyst that acts as a Lewis acid in the Biginelli and Hantzsch reactions [19]. Fee et al. even printed an entire chromatographic column, with the internal column packing, flow connectors and distributors present in the 3D printed column itself [20]. Recent advances by Minas et al. have enabled the printing of highly porous ceramics using emulsions and foams as precursor inks, offering the opportunity to tune the thermal and mechanical properties of such structures by modifying the porosity of the printed struts themselves [21].

At this moment, only a few publications dealing with 3D-printed structures in the field of adsorption are available. Thakkar et al. recently studied $CO_2$ capture by adsorption on 3D-printed zeolite monoliths (5A and 13X) and aminosilica adsorbent structures [22,23]. These 3D-printed adsorbents were based on the deposition of a paste in a layer-by-layer fashion, leading to a well-defined monolith in terms of wall thickness and channel width. The authors concluded that these 3D-printed monoliths are very promising for $CO_2$ capture and thus offer an alternative approach for structuring adsorbents.

In our previous work [24], a 3D-printed monolith of zeolite ZSM-5 was generated by three-dimensional fibre deposition (3DFD) using a 3D-printing method developed by VITO (Vlaams Instituut voor Technologische Ontwikkeling, Belgium) [25,26]. A paste, obtained by mixing the zeolite powder with bentonite, silica and water was printed into an open structure with stacked fibres of 400 μm diameter. This structured adsorbent showed excellent performance in the separation of $CO_2$ from $N_2$ or $CH_4$.

One critical aspect in the development in structured adsorbents is the preparation of the paste that is used in the extrusion or 3D-printing process. It should allow to deposit the structure in a smooth way, but also result in a robust structure that retains a large adsorption capacity. For inorganic porous solids, very often clay or silica based binders or used. Such binder materials require a high temperature treatment to obtain a strong and solid structure. Alternatively, polymeric binders allow to obtain rigid structures without the need for a high temperature treatment. This is interesting when the porous material itself does not withstand such a high temperature treatment.

In this work, we report on the synthesis of a 3D-printed monolith comprising SAPO-34 zeolite, using a polymeric binder material (Methyl cellulose). The monolith is made by printing the zeolite fibres in a layer-upon-layer fashion in a well-defined way. The resulting monolith was tested for adsorption and separation of $CO_2$ and $N_2$ by means of isotherms and breakthrough experiments.

## 2. Materials and methods

### 2.1. Sample preparation

SAPO-34 zeolite (product name: AQSOA Z02) was purchased from Mitsubishi Chemical and used to prepare a paste for 3D-printing. 50 wt% SAPO-34 suspensions were prepared by the addition of the zeolite powder to a 0.6 wt% Polyacrylic acid (Poly(acrylic acid sodium salt), Sigma-Aldrich Chemie GmbH, Germany) solution. In a second type of formulation, 5 wt% graphite (in respect to the SAPO-34 powder) was added to this mixture. Gelation was induced through the incorporation of 2–3 wt% Methylcellulose (Methocel, DOW, Germany) for both formulations.

Cylinders with a diameter of 1 cm and a grid like filling were printed with a speed of 4 mm/s using a pressure-controlled direct ink wiring system (3D Discovery, RegenHu Ltd., Switzerland). A nozzle diameter of 330 μm was used, while the off-set in z-direction was set to 150 μm. Samples were dried at ambient conditions for 48 h.

### 2.2. Characterization and isotherms

The topology of the monoliths, including the size of the channels, the surface of the fibers and agglomeration of the crystals, was analyzed by scanning electron microscopy (JEOL). Ar porosimetry at 87 K was performed with an Autosorb AS-1 from Quantachrome. BET surface area was calculated and pore volume was estimated with the Gurvich rule ($p/p_0 = 0.2$). Low pressure (0–1 bar) $CO_2$ isotherms were determined at different temperatures (273 K–303 K–323 K) with an Autosorb device. Prior to these experiments, the samples were outgassed at a pressure of 0.01 Pa and a temperature of 100 °C overnight, after pre-activation in a vacuum oven. From these isotherm measurements, isosteric heats of adsorption were calculated using the Clausius-Clapeyron equation. The monolithic structures were further characterized with Hg porosimetry (Thermo-Finnigan porosimeter 2000), with a measurement starting at 1 bar and going up to a pressure of 2000 bar. The thermal behaviour was investigated using thermogravimetric (TG) and differential scanning calorimetry (DSC) analysis (SENSYS Evo TG/DSC; SETARAM Instrumentation, France) to determine the heat of adsorption for $CO_2$ on different SAPO-34 samples. An aluminium crucible, filled with SAPO-34 or SAPO-34/graphite monolith sample, was activated at 373 K under an He flow for several hours, and then subjected to a $CO_2$ stream ($P = 1$ bar). High pressure single component isotherms of $CO_2$, $CH_4$ and $N_2$ at 303 K were measured with an automatic gas dosing system and magnetic suspension balance from Rubotherm GmbH. Prior to these measurements, the materials were activated at 373 K under vacuum.

### 2.3. Separation experiments

The separation potential of the monoliths was assessed by performing breakthrough experiments. A detailed description of the setup used for these experiments can be found in earlier work [27]. The amounts adsorbed resulting from the breakthrough times were calculated using the method of Peter et al. [28]. As the monolithic structures were printed with a diameter of 1 cm, they fitted into a 1/2″ stainless steel column. To obtain a reasonable length, different monolith structures were stacked on top of each other to form a length of 5 cm. The different monolith segments were wrapped with Teflon tape in order to avoid gas escaping around the structure. Some monolith segments were also crushed and sieved to obtain 450–600 μm diameter pellets. These pellets were then transferred to a 1/8″ stainless steel column. Breakthrough experiments were conducted with a total flow rate of 40 Nml/min with pure $N_2$ or $CO_2$ or a mixture of those gases. Before each breakthrough experiment, the material was subjected to a temperature increase to 373 K under an inert He flow.

The experimentally obtained selectivity was compared to the selectivity predicated by the Ideal Adsorbed Solution Theory, using the Langmuir fit of the experimental high pressure pure component adsorption isotherm as input to the model [29].

## 3. Result and discussion

In this work, two types of 3D-printed SAPO-34 monoliths were synthesized and tested: a first one containing polyacrylic acid + methylcellulose as binder and a second one which also contains 5 wt% graphite.

Fig. 1 shows pictures of the different monolith structures, ranging from normal sight to a length scale of 5 μm. Each monolith segment is printed with an average length and diameter of 1 cm, as seen in Fig. 1, A. The presence of graphite in one of the monolithic segments gives this monolith a grey colour, in contrast with the white colour of the SAPO-34 monoliths and powder. The fibre thickness is around 300 μm, while the channels have an average width of 650 μm (Fig. 1, B). In Fig. 1 (C–F), a close-up of one fibre clearly reveals the dense stacking of SAPO-34 crystals. As the monoliths are printed with a low amount of binder, no traces of binder are visible in the SEM pictures.

The results from the Ar porosimetry experiments are shown in Fig. 2 (left). The Ar isotherms (left figure) already reveal a notable trend for the normal SAPO-34 monolith. As compared to the powder (left isotherm), the resulting adsorption capacity is much lower than one would expect with only 2% binder present. A decrease of around 50% in capacity was noted for one case (squares in Fig. 2, left). Remark that for the SAPO-34 monolith sample, the Ar isotherm does not close upon desorption even at low pressure. This indicates that some Ar is trapped in the structure and only released at very low pressure. The same phenomenon is found in porous polymer structures. This measurement was repeated with another monolith part (diamonds in Fig. 2, left) and although this resulted in a larger capacity as compared to the first measurement, it still is way lower than expected. The variance between the 2 different monolith parts is a first indication that not every printed monolith segment has the same accessible pore volume with Ar. As for the monolith containing the extra graphite, the decrease in capacity is consistent with the amount of binder and graphite present (8 wt%). It was furthermore noted during the experiments on the SAPO-34 monolith, that at each pressure, uptake of Ar took a very long time and equilibrium was never fully reached in the present experiments. Uptake of Ar was significantly faster on the SAPO-34/graphite monolith or the SAPO-34 powder. This indicates that the

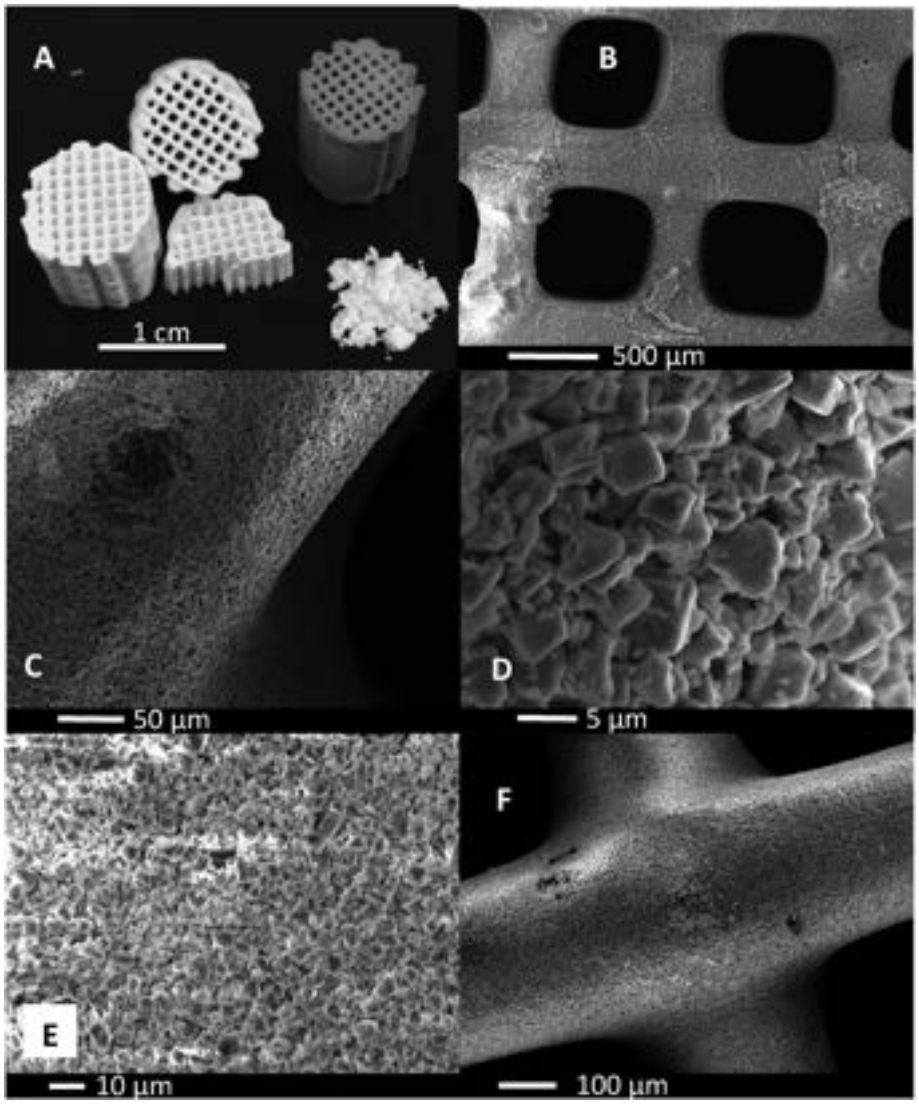


**Fig. 1.** (SEM) pictures of the 3D printed monoliths. A: Several SAPO-34 monolith segments (white) and one SAPO-34/graphite monolith (grey). B to D: SEM pictures of the SAPO-34 monolith in different magnifications (scale bars: 500 μm, 50 μm and 5 μm, respectively). E and F: SEM pictures of the SAP-34/graphite monolith in different magnifications (scale bars: 100 μm and 10 μm).

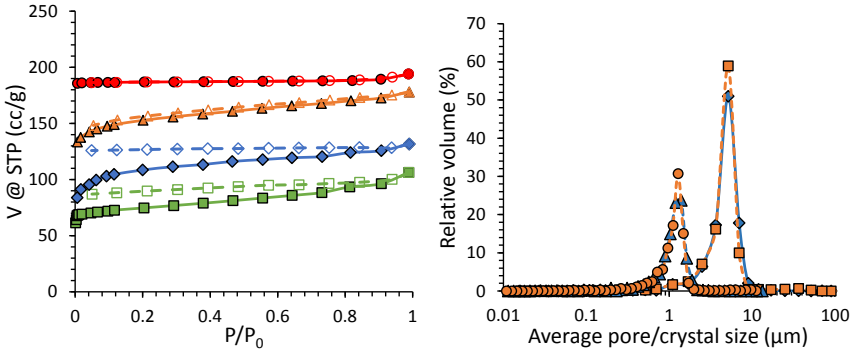


**Fig. 2.** Left: Ar isotherms at 87 K on SAPO-34 powder (●), SAPO-34/graphite monolith (▲), SAPO-34 monolith (from two different segments; ◆ and ■). Closed symbols represents adsorption; open symbols, desorption. Right: pore size distribution (left peak) and crystal size distribution (right peak) on SAPO-34 monolith (blue symbols) and SAPO-34/graphite monolith (orange symbols) as obtained from Hg intrusion experiment. (For interpretation of the references to colour in this figure legend, the reader is referred to the web version of this article.)

SAPO-34 monolith experiences mass-transfer limitations during Ar adsorption. Possibly, the polymeric binder is blocking part of the entrances of the pores, making it difficult for Ar to enter the pores and thus leading to slower adsorption dynamics. The addition of graphite to the monoliths could lead to a better distribution of binder, eliminating the mass transfer problem observed with the SAPO-34 monolith.

Hg intrusion experiments were performed on both monolithic structures to obtain more details about the larger pores (meso- and macropores) present in the monolithic structures. The largest run-through pores cannot be measured with this technique as these large pores are completely filled with Hg before the start of the experiment at the lowest possible pressure. Fig. 2 (right) shows the pore and crystal size distribution of both types of monolith. The curves of both materials practically overlap each other, confirming that both monoliths are similarly printed. The peak in pore size distribution, situated around 1.3 μm and corresponds to the size of the pores formed between the crystals as can also be perceived from the SEM picture (Fig. 1,D). This SEM picture also reveals a crystals size of about 5 μm, which corresponds to the maximum in the particle size distribution as retrieved from the Hg intrusion experiments.

Table 1 summarizes the results from the Ar and Hg porosimetry in terms of BET surface area, pore volumes, crystal size and inter-crystalline pore size. Also here, it is seen that for the SAPO-34 monolith, surface area and pore volume based on the Ar measurement are lower than expected due to the mass transfer limitation.

High pressure isotherms of $CO_2$ on different SAPO-34 structures, obtained with a gravimetric system, are shown in Fig. 3. Different segments of the monoliths were measured. The SAPO-34 and SAPO-34/graphite monoliths labelled “fragment 1” were pristine monolith segments, never used in any other measurement. Fragments denoted with a higher number were retrieved from the breakthrough column and already had a history in $CO_2/N_2$

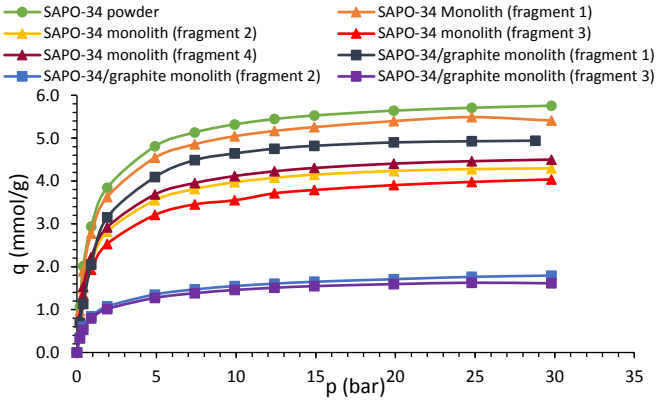


**Fig. 3.** High pressure $CO_2$ isotherms at 303 K on SAPO-34 powder and different monolith fragments (fragment 1 of both SAPO-34 and SAPO-34/graphite monoliths are fresh samples which were never used before, all other fragments were used in breakthrough experiments before isotherm measurement).

separation experiments. When the pristine monoliths are compared to the powder, only a small drop in capacity is noticed, which can be attributed to the presence of binder or binder/graphite in the monoliths. However, a significant drop in capacity is observed on the segments retrieved after the breakthrough experiments. For the SAPO-34 monolith, the average capacity for the samples retrieved after breakthrough is 25% lower as compared to the pristine monolith. For the SAPO-34/graphite monolith, this loss in capacity is even more dramatic, representing a decrease of up to 65%. A possible explanation for this decrease in capacity is the difference in regeneration method. For the isotherm experiments, monoliths are heated under a constant vacuum, while in breakthrough, heating happens under a He flow. During activation in the breakthrough experiments, He flow is lowered to 10 Nml/min to conserve He. Possibly, desorbing water vapour is not removed in an

**Table 1**
Surface area and pore volumes derived from Ar or Hg porosimetry on SAPO-34 powder and monoliths.

| Material | BET surface area ($m^2/g$) | Ar micropore volume (cc/g)[a] (<2 nm) | Hg pore volume (cc/g) (<10 μm) | Pore size between crystals (from Hg) (μm) | Crystal size (from Hg) (μm) |
|---|---|---|---|---|---|
| SAPO-34 Powder | 637 | 0.220 | / | / | / |
| SAPO-34 monolith | 357/263 | 0.134/0.096 | 0.50 | 1.4 | 5 |
| SAPO-34/graphite monolith | 524 | 0.195 | 0.53 | 1.3 | 5 |

[a] Pore volume calculated with the Gurvich rule at $p/P_0$ of 0.2.

efficient way at this low flow rate, which could result in steaming of the zeolite and potential degradation of the material leading to a decreased adsorption capacity. However, performing an extended activation for a longer time did not improve the results. It is, furthermore, also known that certain SAPO-34 samples may degrade after contact with moisture [30,31]. Another observation in Fig. 3 is the large difference in capacity (up to 10%) between several segments of the monolith. Such differences were already noticed in the Ar isotherms (see Fig. 2).

Temperature dependency of the $CO_2$ isotherms on the SAPO-34 and SAPO-34/graphite monoliths was investigated in the low pressure area, as depicted in Fig. 4. Via the Clausius-Clapeyron equation, isosteric heats of adsorption were calculated (Table 2). An independent measurement of the heat of adsorption was obtained via calorimetry (Table 2). Both methods give similar results and show that the heat of adsorption for $CO_2$ is 24–25 kJ/mol for both monoliths.

In order to predict separation potential, single component isotherms for both $CO_2$ and $N_2$ were measured on the SAPO-34 powder and fitted with the Langmuir model (Fig. 5). The obtained Langmuir parameters were used to calculate binary adsorption isotherms for $N_2/CO_2$ mixtures using the IAST method. When an equimolar mixture of $N_2/CO_2$ would be introduced to a SAPO-34 material, IAST predicts that $N_2$ would be practically excluded from the SAPO-34 system and mainly $CO_2$ would be adsorbed, leading to an excellent separation potential. This is clearly seen in Fig. 5, where the dotted lines represent the IAST prediction, while the symbols represent the experimental single component data. At all pressures, $N_2$ adsorption as predicted through IAST is close zero, while the mixture $CO_2$ isotherm nearly coincides with the pure component isotherm. IAST thus predicts a good separation potential of $CO_2$ and $N_2$ on the SAPO-34 material.

Via breakthrough experiments, this separation potential was evaluated in an experimental way. Fig. 6 displays a typical breakthrough profile on a SAPO-34 monolith. $N_2$, as the least adsorbing component, breaks through the column as the first component, while $CO_2$ is retained for significantly longer for this particular breakthrough experiment (equimolar mixture at 1 bar). The $N_2$ profile also shows a distinct roll-up area where adsorbing $CO_2$ is replacing the adsorbed $N_2$, leading to a temporarily increased $N_2$ concentration. With the equation from Peter et al. [28], the amounts of adsorbed gasses were calculated. Due to the large roll-up effect of $N_2$, calculated breakthrough times are slightly negative or barely above zero, resulting in a negative number for the amount of $N_2$ adsorbed (for this reason the $N_2$ results are not displayed in Fig. 7). This confirms the very large selectivity for adsorbing $CO_2$ as predicted by IAST. The amounts of adsorbed $CO_2$ in breakthrough experiments with an equimolar mixture of $CO_2$ and $N_2$ at different total pressures are depicted in Fig. 7 (square symbols). As a reference, single component isotherms from the gravimetric measurements were added, where it was already noticed that a pristine piece of monolith had a higher capacity than the pieces that were retrieved from the breakthrough column (Fig. 3). This is also the case for the capacities calculated from the breakthrough experiments; they are lower than the capacities measured on the pristine material and closer to the isotherm measured on the segments taken from the breakthrough experiments (displayed as the average values of the three separate isotherm measurements).

Apart from the experiments using the complete monoliths, a pristine monolith segment was crushed and sieved to obtain a pellet fraction of 450–600 μm. These pellets were then used to fill a

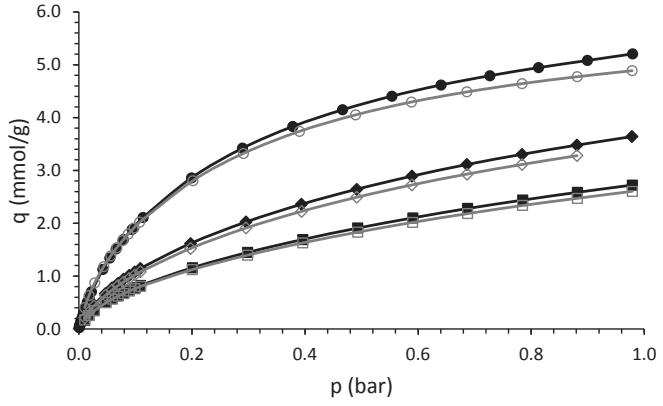


**Fig. 4.** Temperature dependency of the (fresh) SAPO-34 monolith (black curves) and SAPO-34/graphite monolith (grey curves). $CO_2$ isotherms measured at 273 K (circles); 303 K (diamonds) and 323 K (squares).

**Table 2**
Heats of adsorption for $CO_2$, extracted from a calorimeter measurement and from isosteric heat calculations.

| | ΔH (kJ/mol) Calorimetric method | ΔH (kJ/mol) Isosteric method |
|---|---|---|
| SAPO-34 monolith | 24.0 | 23.6 |
| SAPO-34/graphite monolith | 25.0 | 25.0 |

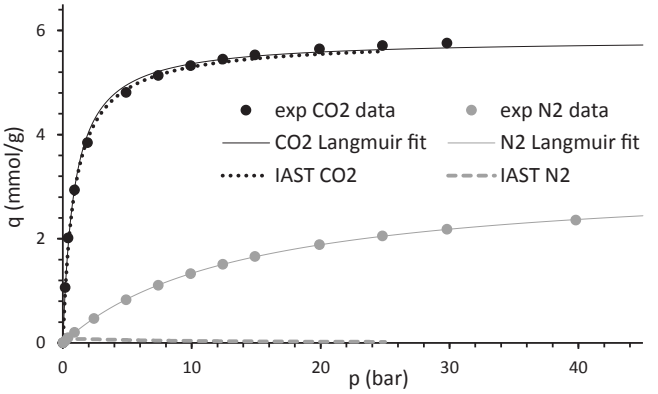


**Fig. 5.** $CO_2$ and $N_2$ isotherms measured on SAPO-34 powder at 303 K. Experimental data (markers) was fitted with a Langmuir model (solid lines) and an IAST model was used to predict the binary isotherms (dotted lines).

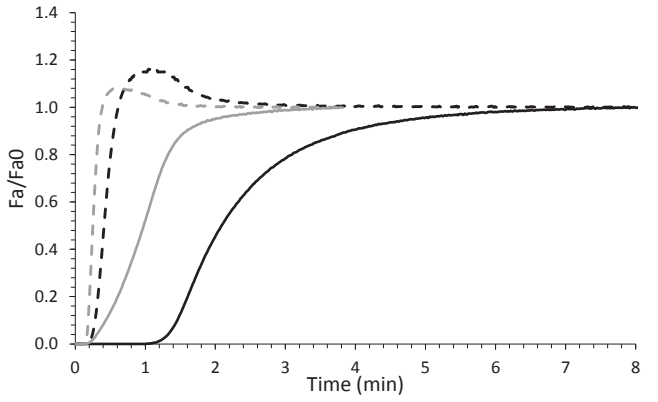


**Fig. 6.** Breakthrough profiles on a SAPO-34 monolith (black) and a SAPO-34/graphite monolith (grey) with a 50/50 mol% $N_2/CO_2$ mixture at 1 bar, 303 K and a total flow of 40Nml/min. Profiles of $CO_2$ are the solid lines, dotted lines are the ones representing $N_2$.

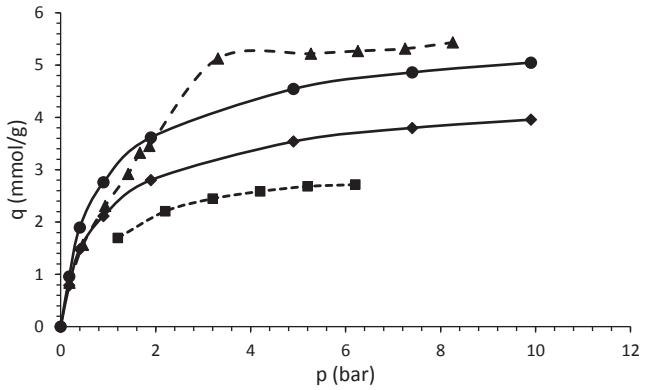


**Fig. 7.** $CO_2$ adsorption capacities of the SAPO-34 monolith calculated from different breakthrough experiments compared to results from gravimetric measurements. ■: Breakthrough results from the SAPO-34 monolith column. ◆: Average gravimetric results from SAPO-34 monolith pieces 2, 3 and 4. ●: Gravimetric result from a pristine SAPO-34 monolith (piece 1). ▲: Breakthrough results from a column filled with crushed monolith (pristine) pieces (450–600 μm). The displayed pressure is the partial pressure of $CO_2$ and not the total pressure of the conducted experiment).

smaller column (length of 15 cm and 1/8″ diameter) as a comparison to the monolith containing column. The $CO_2$ capacities obtained using this pellet containing column are also depicted in Fig. 7 (triangular markers). The $CO_2$ isotherm obtained with the pellet column corresponds well with the gravimetric isotherm obtained with the pristine monolith segment, indicating that the pellet column does not suffer from the capacity decrease that is observed in the breakthrough experiments in the monolithic column. As mentioned before, this decrease in capacity could be due to degradation of the monolith material during activation. With the pellet containing column, gas velocity during activation is more than 1 order of magnitude larger, resulting in a better evacuation of desorbing water. Secondly, part of the decrease in capacity could also be caused by non-isothermal behaviour during the breakthrough experiments caused by the low gas velocity (large column diameter) together with the significant heat of adsorption of $CO_2$. An experiment was conducted to test the importance of thermal effects using one segment of the SAPO-34 monolith. The monolith was suspended in a small container with a gas inlet and outlet; a thermocouple was inserted in one of the pores of the monolith. The container was first flushed with He, subsequently a pure $CO_2$ flow was introduced. Fig. 8 displays the recorded temperature over time and this for both an adsorption and a desorption experiment. When $CO_2$ is adsorbed, the temperature in the monolith starts increasing. After one-and-a-half minute, the monolith reaches its maximum

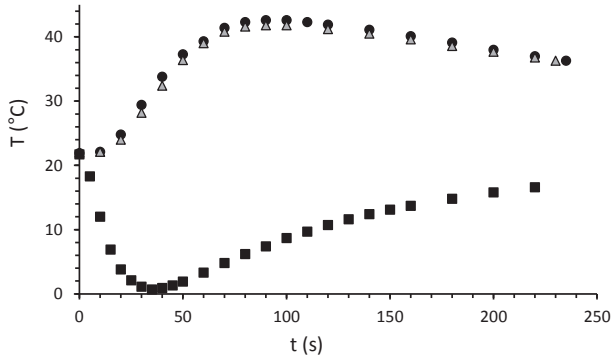


**Fig. 8.** Temperature variation during a $CO_2$ adsorption (● and ▲) and desorption (■) experiment on the SAPO-34 monolith.

temperature of 44 °C, corresponding to an increase of 20 °C. Subsequently, temperature slowly decreases to ambient temperature again. When applying a linear extrapolation (based on the last 6 points in the temperature-time curve) to estimate the time needed to reach ambient temperature again, it would take 9 min. In reality it would take longer to decrease to ambient temperature. At atmospheric conditions, a breakthrough experiment lasts 10–12 min. Hence, the column temperature will be higher than the gas feed temperature, which results in a decreased capacity. This phenomenon at least partially explains the difference between the capacities obtained in breakthrough experiments and in the gravimetric isotherms, where the capacity is measured in equilibrium conditions at a stable temperature.

The breakthrough results for the SAPO-34/graphite monolith were inferior to those obtained on the monolith without graphite, as was already mentioned when isotherms on the different SAPO-34/graphite segments were discussed. In Fig. 6 the breakthrough profiles of an equimolar mixture are visible in comparison with the SAPO-34 monolith breakthrough profiles. As clearly seen, $CO_2$ is almost not retained and starts breaking through at the same time of $N_2$. The goal of adding graphite was to improve the heat conduction in the monolith. The current activation procedure however damaged the material and did not allow for an in depth study of this sample. Future work will be devoted to the study of these 3D-printed SAPO-34 monoliths using a better activation procedure, with special attention to thermal effects. From a practical point of view, towards their implementation in an adsorptive separation process, the reusability (i.e. for several adsorption-desorption cycles), as well as the mechanical strength of the monoliths are additional important aspects to study in the future.

## 4. Conclusions

The highly versatile technique of 3D printing renders it as an ideal method and research tool to develop structured adsorbents for lab scale studies. In this work, SAPO-34 zeolite was used to fabricate two honeycomb-like monolithic structures, one containing methylcellulose as binder, and a second one where extra graphite was added. Both materials showed $CO_2$ adsorption properties similar to the parent powder SAPO-34 with a moderate decrease in capacity due to the presence of binder in the monolithic structures. At low temperature, the presence of the binder resulted in a slow uptake of Ar. While breakthrough experiments demonstrated good performance in the separation of $CO_2/N_2$ gas mixtures, with a very high selectivity for $CO_2$. On the other hand, the adsorption capacity was lower than expected due to thermal effects and material degradation. Nevertheless, the obtained results show that the 3D printing method offers perspectives to develop structured adsorbents in a relative simple manner.

## Acknowledgements

S. Couck and J. Cousin-Saint-Remi are grateful for the financial support of FWO Vlaanderen. C. Minas and P. Ruch acknowledge funding from the Swiss National Science Foundation within the National Research Program 70 (project “THRIVE”, grant no. 153940 and 153989).

## References

[1] F. Rezaei, A. Mosca, J. Hedlund, P.A. Webley, M. Grahn, J. Mouzon, Sep. Purif. Technol. 81 (2011) 191.
[2] P. Avila, M. Montes, E.E. Miro, Chem. Eng. J. 109 (2005) 11.
[3] F. Rezaei, M. Grahn, Ind. Eng. Chem. Res. 51 (2012) 4025.
[4] F. Rezaei, P. Webley, Chem. Eng. Sci. 64 (2009) 5182.
[5] F. Rezaei, P. Webley, Sep. Purif. Technol. 70 (2010) 243.

[6] J. Janchen, T.H. Herzog, K. Gleichmann, B. Unger, A. Brandt, G. Fischer, H. Richter, Microporous Mesoporous Mater. 207 (2015) 179.
[7] R.P.P.L. Ribeiro, C.A. Grande, A.E. Rodrigues, Chem. Eng. Sci. 104 (2013) 304.
[8] C.A. Grande, S. Cavenati, P. Barcia, J. Hammer, H.G. Fritz, A.E. Rodrigues, Chem. Eng. Sci. 61 (2006) 3053.
[9] T.S. Lee, J.H. Cho, S.H. Chi, Build. Environ. 92 (2015) 209.
[10] F. Rezaei, A. Mosca, P. Webley, J. Hedlund, P. Xiao, Ind. Eng. Chem. Res. 49 (2010) 4832.
[11] A. Mosca, J. Hedlund, P.A. Webley, M. Grahn, F. Rezaei, Microporous Mesoporous Mater. 130 (2010) 38.
[12] F. Akhtar, N. Keshavarzi, D. Shakarova, O. Cheung, N. Hedin, L. Bergstrom, Rsc Adv. 4 (2014) 55877.
[13] F.A. Hasan, P. Xiao, R.K. Singh, P.A. Webley, Chem. Eng. J. 223 (2013) 48.
[14] Z.X. Low, Y.T. Chua, B.M. Ray, D. Mattia, I.S. Metcalfe, D.A. Patterson, J. Membr. Sci. 523 (2017) 596.
[15] J. Ruiz-Morales, A. Tarancón, J. Canales-Vázquez, J. Méndez-Ramos, L. Hernández-Afonso, P. Acosta-Mora, J.M. Rueda, R. Fernández-González, Energy & Environ. Sci. 10 (2017) 846–859.
[16] C.W. Hull, US patent 4575330, (1984).
[17] C.R. Tubio, J. Azuaje, L. Escalante, A. Coelho, F. Guitian, E. Sotelo, A. Gil, J. Catal. 334 (2016) 110.
[18] P. Michorczyk, E. Hedrzak, A. Wegrzyniak, J. Mater. Chem. A 4 (2016) 18753.
[19] J. Azuaje, C.R. Tubio, L. Escalante, M. Gomez, F. Guitian, A. Coelho, O. Caamano, A. Gil, E. Sotelo, Appl. Catal. General 530 (2017) 203.
[20] C. Fee, S. Nawada, S. Dimartino, J. Chromatogr. A 1333 (2014) 18.
[21] C. Minas, D. Carnelli, E. Tervoort, A.R. Studart, Adv. Mater. 28 (2016) 9993.
[22] H. Thakkar, S. Eastman, A. Hajari, A.A. Rownaghi, J.C. Knox, F. Rezaei, Acs Appl. Mater. Interfaces 8 (2016) 27753.
[23] H. Thakkar, S. Eastman, A. Al-Mamoori, A. Hajari, A.A. Rownaghi, F. Rezaei, ACS Appl. Mater Interfaces 9 (2017) 7489.
[24] S. Couck, J. Lefevere, S. Mullens, L. Protasova, V. Meynen, G. Desmet, G.V. Baron, J.F.M. Denayer, Chem. Eng. J. 308 (2017) 719.
[25] J. Van Noyen, A. De Wilde, M. Schroeven, S. Mullens, J. Luyten, Int. J. Appl. Ceram. Technol. 9 (2012) 902.
[26] M. Rombouts, S. Mullens, J. Luyten, P. Nuyts, M. Schroeven, Innovative Dev. Des. Manuf. Adv. Res. Virtual Rapid Prototyp. (2010) 453.
[27] S. Couck, E. Gobechiya, C.E.A. Kirschhock, P. Serra-Crespo, J. Juan-Alcaniz, A.M. Joaristi, E. Stavitski, J. Gascon, F. Kapteijn, G.V. Baron, J.F.M. Denayer, Chemsuschem 5 (2012) 740.
[28] S.A. Peter, G.V. Baron, J. Gascon, F. Kapteijn, J.F.M. Denayer, Adsorpt. J. Int. Adsorpt. Soc. 19 (2013) 1235.
[29] A.L. Myers, J.M. Prausnitz, Aiche J. 11 (1965) 121.
[30] M. Briend, R. Vomscheid, M.J. Peltre, P.P. Man, D. Barthomeuf, J. Phys. Chem. 99 (1995) 8270.
[31] J. Cousin Saint Remi, A. Lauerer, C. Chmelik, I. Vandendael, H. Terryn, G.V. Baron, J.F.M. Denayer, J. Kärger, Nat. Mater. 15 (2016) 401.